INVITED PAPER

III-V Infrared Research at the Jet Propulsion Laboratory

S. D. Gunapala, *Fellow SPIE,* D. Z. Ting, C. J. Hill, A. Soibel, John Liu, J. K. Liu, J. M. Mumolo, S. A. Keo, and J. Nguyen
Jet Propulsion Laboratory, California Institute of Technology, Pasadena, California
S. V. Bandara
Night Vision and Electronic Sensors Directorate, Fort Belvoir, Virginia
M. Z. Tidrow, *Fellow SPIE*
Missile Defense Agency/AS, 7100 Defense Pentagon, Washington, DC

ABSTRACT

Jet Propulsion Laboratory is actively developing the III-V based infrared detector and focal plane arrays (FPAs) for NASA, DoD, and commercial applications. Currently, we are working on multi-band Quantum Well Infrared Photodetectors (QWIPs), Superlattice detectors, and Quantum Dot Infrared Photodetector (QDIPs) technologies suitable for high pixel-pixel uniformity and high pixel operability large area imaging arrays. In this paper we report the first demonstration of the megapixel-simultaneously-readable and pixel-co-registered dual-band QWIP focal plane array (FPA). In addition, we will present the latest advances in QDIPs and Superlattice infrared detectors at the Jet Propulsion Laboratory.

Keywords: infrared detectors, infrared imaging, quantum well devices

1. QUANTUM WELL INFRARED PHOTODETECTOR (QWIP)

Single-band Quantum well infrared photodetectors (QWIPs) are well known for their ease of fabrication, ruggedness, pixel-to-pixel uniformity and high pixel operability [1]. QWIP is based on a resonant absorption between ground state and a quasi-continuum state. The spectral response of QWIPs are inherently narrow-band and the typical full-width at half-maximum (FWHM) is about 10% of the peak wavelength. This makes it suitable for fabrication of negligible optical cross-talk dual-band detector arrays.

There are many applications that require mid-wavelength infrared (MWIR) and long-wavelength infrared (LWIR) dual-band focal plane arrays (FPAs). For example, a dual-band FPA camera would provide the accurate temperature [2] of a target with unknown emissivity which is extremely important to the process of identifying objects based on their surface temperature. Dual-band infrared FPAs can also play many important roles in Earth and planetary remote sensing, astronomy, etc. Furthermore, monolithically integrated pixel co-located simultaneously readable dual-band FPAs eliminate the beam splitters, filters, moving filter wheels, and rigorous optical alignment requirements imposed on dual-band systems based on two separate single-band FPAs or a broad-band FPA system with filters. Dual-band FPAs also reduce the mass, volume, and power requirements of dual-band systems. Due to the inherent properties such as narrow-band response, wavelength tailorability, and stability (i.e., low 1/f noise) associated with GaAs based QWIPs [1], it is an appropriate detector choice for large format dual-band infrared FPAs.

2. DUAL-BAND QWIP DEVICE

As shown in Fig. 1, our dual-band FPA is based on two different types of (i.e., MWIR and LWIR) QWIP devices separated by a 0.5 μm thick, heavily doped, n-type GaAs layer. One can stack the MWIR and LWIR multi-quantum-well (MQW) structures in different ways. The device structure shown in Fig. 1(a) is commonly used and described in reference [3]. Fig. 1 (b) –(c) are novel and these structures have two heavily doped GaAs contact layers between MWIR and LWIR MQW regions and an undoped AlGaAs layer embedded between these two GaAs contact layers.

Device structure in Fig. 1 (b) uses two separate detector-common (or ground) contacts, which are connected via the read out integrated circuit (ROIC). Also, it is worth noting in this structure that MWIR and LWIR detectors operate with opposite polarities. Fig. 1 (c) shows a similar device structure to Fig. 1 (b), the only difference is both the MWIR and LWIR device will operate on the same polarity. Fig. 1 (d) shows an interesting dual-band device structure that uses only two indium bumps per pixel compared to three indium bumps per pixel with all pixel co-located dual-band devices [3]. In this device structure the detector-common is shorted to the bottom detector-common plane via a metal bridge. Thus, this device structure reduces the number of indium bumps by 30% and has a unique advantage in large format FPAs, since more indium bumps require additional force during the FPA hybridization process.

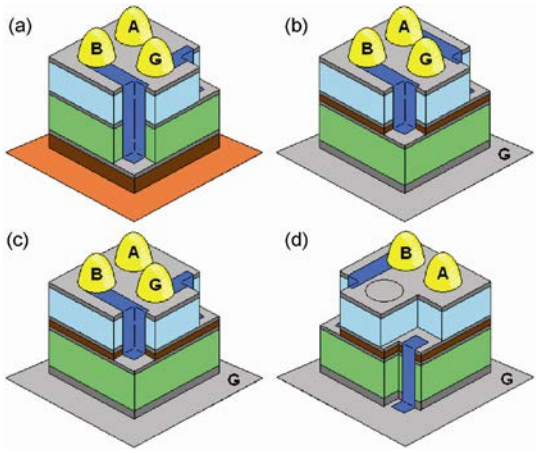

Fig 1. 3-D view of four possible dual-band QWIP device structure showing via connects for independent access of MWIR and LWIR devices. The color code is as follows, orange - isolation layer; green - LWIR QWIP; light blue - MWIR QWIP; grey - contact layer; dark blue - metal bridges between MQW regions; yellow - indium bumps.

A coupled-quantum well structure was used in this device to broaden the responsivity spectrum. In the MWIR device, each period of the MQW structure contains a 300 Å thick un-doped barrier of $Al_{0.25}Ga_{0.75}As$, and a double quantum well region. The double QW region contains two identical quantum wells separated by a 45 Å of Al0.25Ga0.75As un-doped barrier. Each of the two quantum wells consists of 3 Å AlAs, 5 Å GaAs, 32 Å $In_{0.3}Ga_{0.7}As$, 5 Å GaAs, and 3 Å AlAs; the quantum well is doped n = $4x10^{18}$ cm–3. This period was repeated 13 times. In the LWIR device, each period of the MQW structure contains a 580 Å thick un-doped of $Al_{0.25}Ga_{0.75}As$ barrier, and a triple quantum well region. The triple QW region contains three identical 50 Å GaAs quantum wells (doped to n = $5x10^{17}$ cm–3) separated by 50 Å of $Al_{0.25}Ga_{0.75}As$ un-doped barriers. This period was repeated 16 times. These two photosensitive MQW structures are sandwiched between GaAs top and bottom contact layers doped n = $1x10^{18}$ cm–3, grown on a semi-insulating GaAs substrate by molecular beam epitaxy (MBE). Top contact was a 0.7 μm thick GaAs cap layer on top of a 350 Å $Al_{0.25}Ga_{0.75}As$ stop-etch layer grown in situ on top of the dual-band device structure to fabricate the light coupling optical cavity. The bottom contact layer was a 2 μm thick GaAs layer. A 0.4 μm thick un-doped AlGaAs layer was embedded between the top contact of the LWIR and bottom contact of the MWIR MQW regions. As shown in Fig. 2, the MWIR device uses a bound-to-continuum design to help further broaden the spectrum; a single monolayer of AlAs on each side of quantum well is used to help increase the oscillator strength. The LWIR device uses a standard bound-to-quasibound design, where the upper levels involved in the infrared optical transition is in approximate resonance with the conduction band edge of the barrier. Note that the same AlGaAs barrier composition is used throughout the structures.

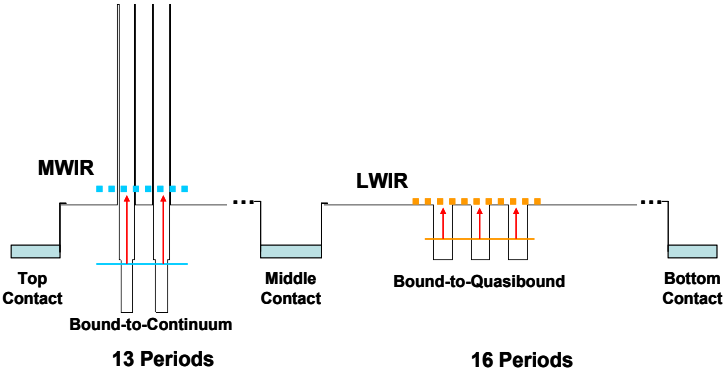

Fig 2. Energy band diagram of the dual-band QWIP structure.

The MBE grown material was tested for absorption efficiency using a Fourier Transform Infrared (FTIR) spectrometer. The experimentally measured peak absorption (or internal) quantum efficiency (η_a) of this material at room temperature was 19%. The epitaxially grown material was processed into 200 μm diameter mesa test structures (area = 3.14×10^{-4} cm^2) using wet chemical etching, and Au/Ge ohmic contacts were evaporated onto the top and bottom contact layers. The detectors were back illuminated through a 45° polished facet and a responsivity spectrum is shown in Fig. 3. The responsivity of the detector peaks at 4.6 μm and the peak responsivity (R_p) of the detector is 170 mA/W at bias $V_B = -1$ V. The spectral width and the cutoff wavelength are $\Delta\lambda/\lambda = 15\%$ and $\lambda_c = 5.1$ μm respectively.

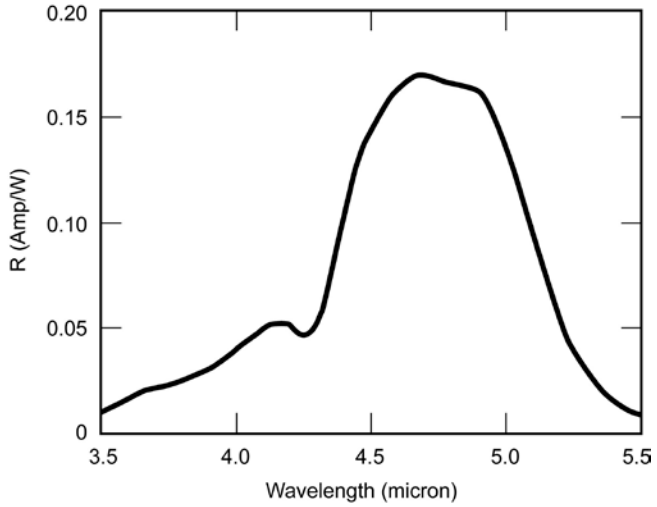

Fig. 3. Responsivity spectrum of a bound-to-quasi-bound MWIR QWIP test structure at temperature T = 77 K. The spectral response peak is at 4.6 μm and the long wavelength cutoff is at 5.1 μm.

The experimentally measured LWIR responsivity spectrum is shown in Fig. 4. The responsivity of the detector peaks at 8.4 μm and the peak responsivity (R_P) of the detector is 130 mA/W at bias $V_B = -1$ V. The spectral width and the cutoff wavelength are $\Delta\lambda/\lambda = 10\%$ and $\lambda_c = 8.8$ μm, respectively.

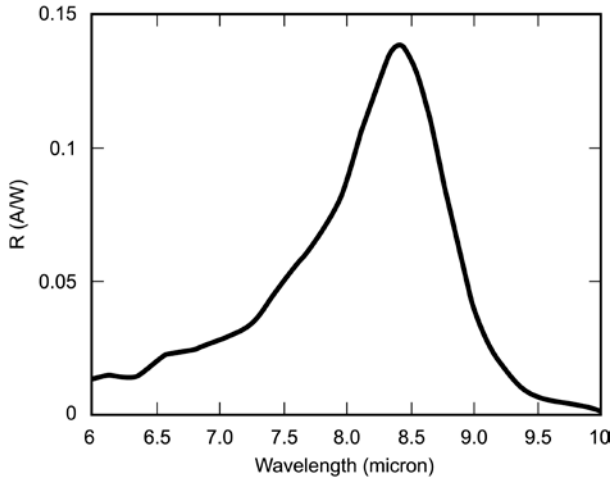

Fig 4. Responsivity spectrum of a bound-to-quasibound LWIR QWIP test structure at temperature T = 77 K. The spectral response peak is at 8.4 μm and the long wavelength cutoff is at 8.8 μm.

3. 1024X1024 PIXEL DUAL-BAND QWIP FOCAL PLANE ARRAY

After the light coupling 2-D grating array was defined by stepper based photolithography and dry etching, the MWIR detector pixels of the 1024x1024 pixel detector arrays, and the via-holes to access the detector-common, were fabricated by dry etching through the photosensitive GaAs/$In_yGa_{1-y}As$/$Al_xGa_{1-x}As$ MQW layers into the 0.5 μm thick doped GaAs intermediate contact layer. Then LWIR pixels and via-holes for MWIR pixels to access the array detector-common were fabricated. A thick insulation layer was deposited and contact windows were opened at the bottom of each via-hole and on the top surface. Ohmic contact metal was evaporated and unwanted metal was removed using a metal lift-off process. The pitch of the detector array is 30 μm and the actual MWIR and LWIR pixel sizes are 28x28 μm^2. Five detector arrays were processed on a four-inch GaAs wafer. Indium bumps were then evaporated on top of the detectors for hybridization with ROICs. Several dual-band detector arrays were chosen and hybridized (via an indium bump-bonding process) to grade A 1024x1024 pixel dual-band silicon ROICs. Fig. 5 shows a megapixel dual-band QWIP FPA mounted on a 124 pin LCC.

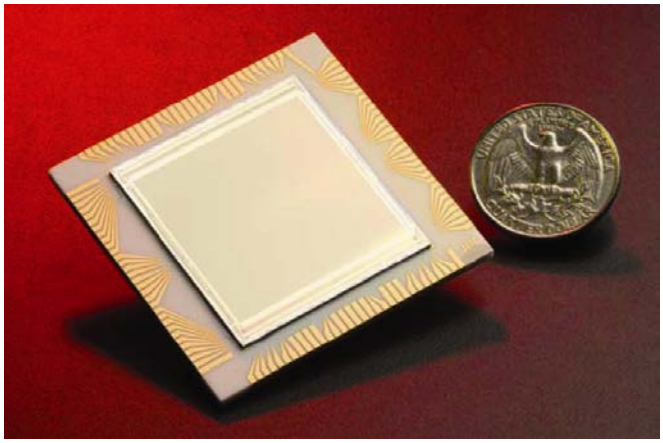

Fig. 5. Picture a 1024x1024 pixel dual-band QWIP FPA mounted on a 124-pin lead less chip carrier.

A MWIR:LWIR pixel co-registered simultaneously readable dual-band QWIP FPA has been mounted onto the cold finger of a pour fill dewar, cooled by liquid nitrogen, and the two bands (i.e., MWIR and LWIR) were independently

biased. Some imagery was performed at a temperature of 68 K. An image taken with the first megapixel simultaneous pixel co-registered MWIR:LWIR dual-band QWIP camera is shown in Fig.6.

Fig. 6. An image taken with the first megapixel simultaneous pixel co-registered MWIR:LWIR dual-band QWIP camera. The flame in the MWIR image (left) looks broader due to the detection of heated CO_2 (from cigarette lighter) re-emission in 4.1–4.3-micron band, whereas the heated CO_2 gas does not have any emission line in the LWIR (8–9 microns) band. Thus, the LWIR image shows only thermal signatures of the flame.

This initial array gave good images with 99% of the MWIR and 97.5% of the LWIR pixels working in the center 512x512 pixels region, which is excellent compared to the difficultness in the fabrication process of this pixel co-registered simultaneously readable dual-band QWIP FPA. The digital acquisition resolution of the imaging system was 14-bits, which determines the instantaneous dynamic range of the camera (i.e., 16,384). However, the dynamic range of QWIP is 85 Decibels. Video images were taken at a frame rate of 30 Hz at temperatures as high as T = 68 K. The total ROIC well depth is $17x10^6$ electrons with LWIR to MWIR well depth ratio of 4:1. The estimated NEΔT based on single pixel data of MWIR and LWIR detectors at 68 K are 22 and 24 mK, respectively. The measured mean NEΔT was estimated at 27 and 40 mK for MWIR and LWIR bands respectively at a flat plate blackbody temperature of 300K with f/2 cold stop.

The experimentally measured NEΔT histograms distributions at blackbody temperature of 300 K with f/2 cold stop are shown in the Fig. 7 (a) and (b). The experimentally measured MWIR NEΔT value closely agrees with the estimated NEΔT value based on the results of a single element test detector data. However, the measured LWIR NEΔT value is higher than the estimated NEΔT value based on the single pixel data. This is due to the fact that we could not completely independently optimize the operating bias of LWIR band due to a ROIC pixel short circuit occurred at the MWIR band.

The operability was defined as the percentage of pixels having NEΔT within 3σ of the NEΔT histograms taken at 300 K background with f/2 cold shield. However, the pixel operability dropped to approximately 90% for both bands with full frame. The poor pixel operabilities of both bands are due to via-metal bridge breakage. These metal layers were deposited via e-beam metal evaporation. We think this metal breakage issue can be solved with sputtering based metal deposition due to its conformal coverage. Array non-uniformities before correction were 22% and 20% for MWIR and LWIR bands respectively. After two-point corrections non-uniformities were reduced to about 1%. The dual-band image shown in Fig. 6 was taken with full frame after two-point correction. High array non-uniformity and low pixel operability are directly related to the metal connections fabricated through via-holes. Pixel co-located dual-band array process (thirteen layer photolithography) is much more complicated compared to the single-band QWIP detector array process (three layer photolithography.

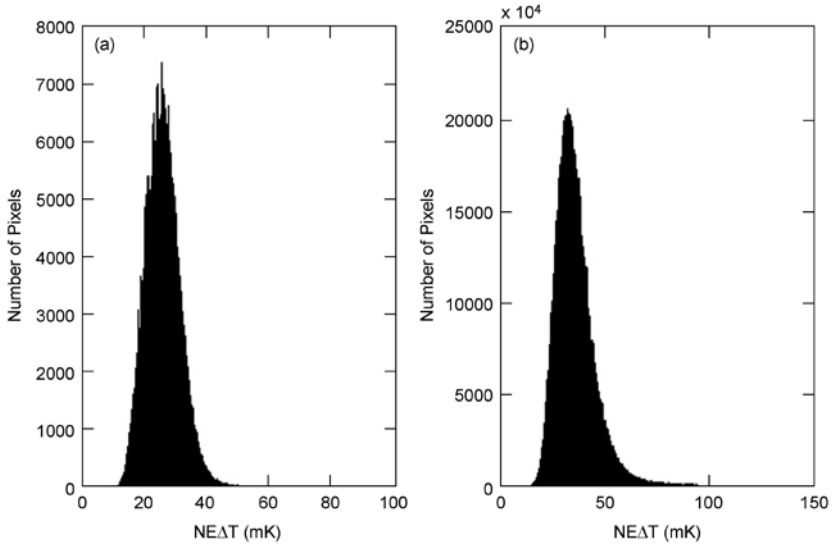

Fig. 7. NEΔT histogram of the 1024x1024 format simultaneously readable pixel co-registered dual-band QWIP FPA. Each spectral band of the FPA consisted of co-registered megapixel.

As we have mentioned earlier, QWIP is a good detector choice for the fabrication of pixel co-registered simultaneously readable dual-band infrared focal plane arrays due to its narrow spectral band spectral response. Thus it provides negligible spectral cross-talk when two spectral bands are a few microns apart. The initial GaAs substrate of these dual-band FPAs are completely removed leaving only a 50 nm thick GaAs membrane. Thus, these dual-band QWIP FPAs are not vulnerable to FPA de-lamination and indium bump breakage during thermal recycling process, and have negligible pixel-to-pixel optical cross-talk. We feel that FPA non-uniformity and associated spatial noise could be significantly reduced by improving the detector array processing and optimizing the ROIC.

4. QUANTUM DOT INFRARED PHOTODETECTOR (QDIP)

The artificial atom-like properties of epitaxially self-assembled quantum dots (QDs) were exploited in this work for the development of large-format, long wavelength infrared (LWIR) focal plane arrays (FPAs) with high operability and spatial uniformity. QDs are nanometer-scale islands that form spontaneously on a semiconductor substrate due to lattice mismatch. QD infrared photodetectors (QDIPs) with properly engineered dots have been predicted theoretically to have significant advantages over quantum well infrared detectors (QWIPs) [5]. QDIPs are fabricated using robust wide band gap III-V materials which are well suited to the production of highly uniform LWIR arrays. QD based infrared photodetectors have the potential to make a significant impact on the next generation of infrared imaging systems. QDIPs possess all of the advantages of traditional III-V based infrared photodetectors, such as: extremely high operability, mature fabrication technology, very large formats, and material production that is increasingly high volume and low cost. The addition of active nanoscale particles (i.e. QDs) embedded within the III-V infrared detector allows for higher operating temperatures and increased band gap tunability without sacrificing the economic advantages of the mature III-V infrared imaging system pipeline.

The main benefit in using the QD approach stems from 3D quantum confinement, which (1) enables normal incidence absorption by modifying the optical transition selection rule, and, (2) increases the photo-excited carrier lifetime by reducing optical phonon scattering via the “phonon bottleneck” mechanism [5]. However, QDs also have some drawbacks that need to be addressed. In a typical detector structure, QD densities are low (compared to the number of dopants in the active regions of QWIPs); so while individual QDs are efficient absorbers, typical QD densities are not high enough to achieve high quantum efficiency. Thus, while QD based infrared detectors have

clearly demonstrated normal incidence absorption [5-6], and, in some instances, higher operating temperature as well [5], they are still lacking in quantum efficiency and responsivity.

5. THE DOT-IN-THE-WELL INFRARED PHOTODETECTOR

The first-generation QDIPs are high-gain, low-quantum-efficiency devices. Improving quantum efficiency is a key to achieving a competitive QD-based FPA technology. This can be accomplished by increasing the QD density, or by enhancing the infrared absorption in the QD-containing material. There are various versions of QDIPs, based on different materials and designs. Thus, application engineers have a choice of devices to select from for their applications. The particular application which we are interested in is remote sensing of planetary atmospheres. The tailorability of the FPA cut-off wavelength is important in this application. We chose the Dot-in-a-well (DWELL) QDIP device structure shown in Fig. 8 for the ease of wavelength tunability (see Fig. 9). Our specific implementation uses InAs QDs embedded in InGaAs/GaAs multi-quantum well structures, as illustrated in Fig. 8. It has been shown that this material system can support a large number of QD stacks without suffering material degradation, thereby allowing high dot density. The host InGaAs/GaAs multi-quantum well structures are highly compatible with the mature FPA fabrication process that are used routinely to make QWIP FPAs. Similar to other intersubband detectors, DWELLs operate by the photoexcitation of electrons between energy levels in the potential well created by the nano-scale QD in a well structure. The right panel of Fig. 8 shows that, under an applied bias voltage, these photo-excited carriers can escape from the potential wells and be collected as photocurrent. The wavelengths of the spectral peaks (λ_p) are determined by the energy difference between quantized states in the DWELL. The hybrid quantum-dot/quantum-well, or dot-in-a-well, device offers two advantages: (1) challenges in wavelength tuning through dot-size control can be compensated in part by engineering the quantum well sizes, which can be controlled precisely; (2) quantum wells can trap electrons and aid in carrier capture by QDs, thereby facilitating ground state refilling [5]. The advantage is that it would increase the absorption quantum efficiency. But on the other hand, DWELL QDIPs have lower gain than conventional QDIPs due to carrier trapping by the quantum wells. In traditional QDIPs, the large photoconductive gain could lead to higher operating temperature due to the lowering of dark current. The trade-off for DWELL QDIPs is the sacrifice in gain for higher quantum efficiency.

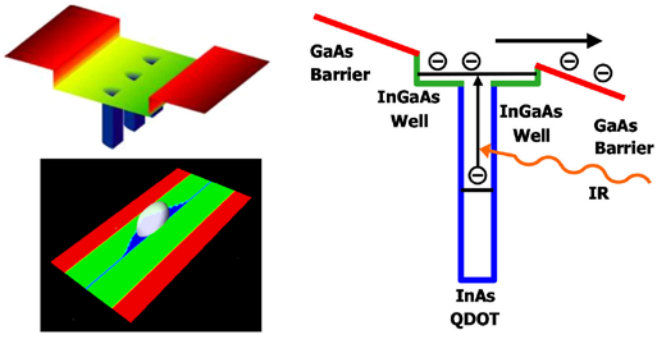

Fig. 8. Illustration of the Dot-in-a-Well (DWELL) device. Top left panel shows the potential profile, with three pyramid shaped dots embedded in the quantum well. The bottom left panel displays a calculated DWELL ground state wave function, represented by a white translucent equal-probability isosurface, localized by a pyramidal quantum dot. The right panel illustrates the operation of a DWELL infrared detector.

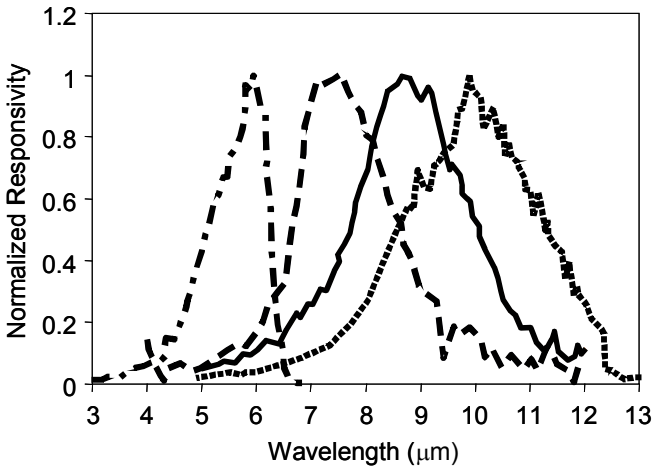

Fig. 9. Experimentally measured spectral responsivity of DWELL QDIPs demonstrating spectral tunability by varying the well width from 55 Å to 100 Å.

6. VI. QUANTUM DOT MATERIAL GROWTH

QDs can be fabricated by taking advantage of a strain-induced transformation that happens naturally in the initial stages of epitaxial growth for lattice-mismatched materials. One highly successful method of achieving QDs is through self-organized growth in the Stranski-Krastanow growth mode [5]. Similar to quantum wells, these structures are fabricated by MOCVD or MBE using III-V materials (e.g., InGaAs/AlAs/GaAs/InAs). Three-dimensional islands can be formed spontaneously during strained layer epitaxy, and they exhibit fairly good uniformity in size, shape and spatial distribution. By using a smaller band gap material (InAs) for the strained layer to form the 3D nanostructures and a larger band gap material for the barrier (InGaAs, GaAs, or AlGaAs), three-dimensional carrier confinement can be achieved.

Our growth procedure follows closely that for the DWELL structures reported in the literature [5]. In the sample used for the FPA demonstration, the InAs QDs were grown in the center of a 75Å $In_{0.12}Ga_{0.88}As$ quantum well at a substrate temperature of 490°C. Ground state electrons were provided to the detector by doping the InAs with Si to a density of $5x10^{17}cm^{-3}$. The approximate dot density is $3x10^{10}cm^{-2}$, as determined by AFM of uncapped layers. We note, however, the dot density of the capped layers may differ due to segregation and diffusion. The quantum wells were separated by 500Å of undoped GaAs. We have increased the overall number of photosensitive DWELL stacks to 30. This has led to much higher quantum efficiency in our structures than previously reported values for DWELL QDIP structures [5]. This photosensitive DWELL structure is sandwiched between 0.66 μm GaAs top and 0.5 μm bottom contact layers doped n = $5x10^{17}$ cm^{-3}. All DWELL-QDIP wafers were grown on semi-insulating 75 mm GaAs substrates.

7. TEST DETECTOR FABRICATION

After evaluating material quality, selected wafers were processed into 200 μm x 200 μm test detector mesas. DWELL QDIP test detectors were fabricated by standard wet and dry chemical etching through the stack of photosensitive layers into the doped GaAs bottom contact layer. The top of the detectors was covered with Au/Ge and Au for an Ohmic contact, which also serves as a reflector for light incident through the bottom contact, allowing two passes through the active layers. Initial QDIP characterization of discrete devices included measurements of the room-temperature absorption spectra, side [5] and normal incident responsivity spectra, dark current, and noise. These detectors were tested in a cryogenically cooled test bed using a calibrated blackbody source to evaluate the responsivity of the detector over the relevant range of operating temperatures and bias voltages. The test results were used to verify and adjust the model used in designing the material parameters. This cycle was iterated several times in order to develop the recipe for the final optimized detector wafer used to make FPAs.

8. DWELL QDIP ABSORPTION QUANTUM EFFICIENCY

A separate 8-pass polished waveguide structure was fabricated for absorption measurements [5]. Fig. 3 shows the measured absorption quantum efficiency from a 30-stack DWELL QDIP, with a peak value at approximately 2.7%. To our knowledge, this is the highest measured intrinsic absorption quantum efficiency published to date in a QD based LWIR infrared detector. A typical set of results on measured normal and 45-degree incidence responsivity of the DWELL QDIP samples are shown in Fig. 10. It is found that the normal incidence responsivity (relative to the 45-degree responsivity) is much stronger (almost 1 order of magnitude) than that for the typical QWIP. At the same time, we also find that the 45-degree incidence responsivity is 4 to 5 times stronger than the normal incidence responsivity. This observation is consistent with our simulation results [5]. In the typical InAs/(In)GaAs QDIP, the dot base width is much larger than the dot height. In such low-aspect-ratio dots, while the ground to the first excited state transition can produce strong normal incidence absorption, it does not contribute appreciably to the photocurrent under small or moderate biasing conditions because the first excited state is deeply bound. Instead, the typical observed photo-response is due to transition to higher excited states, and such transitions could be induced by either normal-incidence or inclined incidence light, depending on the symmetry of the states involved in the optical transition. It should be noted that this observed property is not specific to the DWELL QDIP; similar theoretical and experimental results on conventional InAs/GaAs QDIPs have also been reported [5].

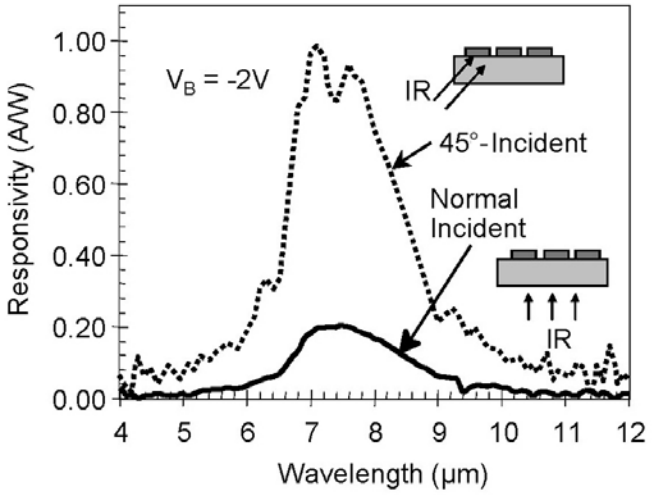

Fig. 10. DWELL QDIP spectral responsivity measured for (a) normal incidence, (b) 45° incidence.

Fig. 10 indicates that at wavelength range shown, our DWELL QDIPs have reasonable absorption strength for normal-incidence light (x,y-polarized; with z being the normal incidence direction), but also absorbs inclined (or side) incidence (z-polarized) light even more strongly. Accordingly, we designed a reflection grating structure to take advantage of the detector's ability to absorb both normal and inclined incidence light in order to maximize quantum efficiency. As in QWIPs, normal incidence light can be coupled to the z-polarization light absorption mechanism in DWELL QDIPs by using a reflection grating. For this experiment we grew a separate sample, with a slightly adjusted well structure. Fig. 11 shows our measured results on grating enhancement. Normal incidence responsivity was measured for the DWELL QDIP sample, fabricated both with and without a reflection grating. The device with the reflection grating shows almost four times larger normal incident responsivity than the one without, clearly indicating the promise of this approach.

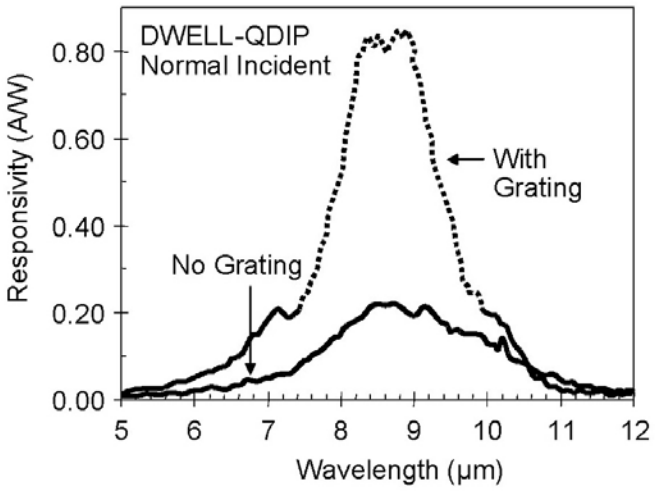

Fig. 11. Normal incidence spectral responsivity of a DWELL-QDIP with and without reflection gratings.

Given that the gain of DWELL QDIPs is quite different (typically less than 1) from other intersubband detectors, it is worthwhile to examine how this affects the detector performance. The sensitivity of DWELL QDIPs can be evaluated by measuring parameters such as absolute spectral responsitivity $R(\lambda)$, absorption quantum efficiency (internal) η, photocurrent (I_P), dark current I_D, noise current i_n, and specific detectivity (D^*). Similar to other intersubband photodetectors, these parameters are linked to each other through the photoconductive gain (g) of the detector, $R = e\eta g/(hc/\lambda)$, $i_n = \sqrt{4e(I_D + I_P)g\Delta f}$, and $D^* = R\sqrt{A\Delta f}/i_n$ [5]. Here, e is the electron charge, Δf is the bandwidth, A is the detector area, and hc/λ is the photoexcitation energy. When the detector operates in background limited conditions ($I_P >> I_D$), since I_P is proportional to gain, D^* depends only on the absorption quantum efficiency η, regardless of the size of the photoconductive gain. Therefore, improving absorption quantum efficiency is the key to improving the ultimate performance of these detectors for background limited operation [5]. Detectivity D* of this detector as a function of device temperature at operating bias V_B = -1V was experimentally obtained and it reached background limited $D^* \sim 1\text{x}10^{11}$ Jones around T = 50 K temperature. In the future, we expect to improve D* through reduction of dark current and increase in quantum efficiency. Specifically, (1) dark current reduction would extend the plateau of the BLIP (background limited performance) D* curve to higher temperature, (2) quantum efficiency increase would shift the BLIP D* curve upward over the entire temperature range. Further reduction in dark current would help to achieve BLIP performance at higher operating temperatures.

9. FOCAL PLANE ARRAY FABRICATION

After establishing optimized layer thickness and growth conditions for the LWIR DWELL-QDIP, the FPA material was grown on 75 mm semi-insulating GaAs substrates. Selected wafers were processed into FPAs. After the 2D grating array was defined by photolithography and dry etching, the LWIR detector pixels of the 640x512 FPAs were fabricated by dry etching through the photosensitive GaAs/$In_xGa_{1-x}As$/InAs layers into the 0.5 μm thick doped bottom GaAs (i.e., detector common) layer. The pitch of the FPA is 25 μm, and the actual QDIP pixel size is 23x23 μm^2. The 2D grating reflectors on top of the detectors were then covered with Au/Ge and Au for Ohmic contact and reflection. Twelve FPAs were processed on a 75 mm GaAs wafer. Indium bumps were then evaporated on top of the detectors for silicon read out integrated circuit (ROIC) hybridization. Several FPAs were chosen and hybridized (via an indium bump-bonding process) to a 640x512 pixel direct injection CMOS ROIC (ISC-9803).

After the 640x512 pixel QDIP detector arrays were hybridized to a 640x512 pixel ROIC, a simple electronic functionality test was performed to evaluate the FPAs. Then we thinned the selected FPA hybrids by removing the entire substrate while leaving the detector pixels, the bottom contact layer and the dielectric mirror. During thinning, the entire substrate material was removed by abrasive polishing, wet chemical etching followed by dry etching that

ends at the epitaxially grown selective etch layer. This thinned detector array completely eliminates the thermal mismatch issue between the CMOS ROIC and the GaAs/InAs/AlAs based detector array, pixel outages, and pixel-to-pixel optical cross talk of the FPA. Basically, the thinned GaAs based QDIP FPA membrane adapts to the thermal expansion and contraction coefficients of the silicon ROIC. Thus, thinning has played an extremely important role in the fabrication of large area FPA hybrids. Elimination of thermal mismatch is a process of paramount importance in achieving high quality, large area FPAs without pixel delamination [5]. Another important consequence of the thinning process is that the thinned structure effectively forms a wavguide that serves to enhance the optical field, thereby increasing the absorption quantum efficiency.

10. QDIP FOCAL PLANE ARRAY DEMONSTRATION

Selected detector hybrids were mounted and wire-bonded to a leadless chip carrier (LCC). A specially designed dewar was used to characterize the FPA functionality using a general-purpose electronic system from SE-IR Incorporated. The SE-IR system was programmed to generate complex timing patterns, and was reconfigured to handle a development grade FPAs. The best performance was determined by optimizing operating-parameters for each FPA. The FPAs were characterized for pixel responsivity, quantum efficiency, noise, D^*, NEΔT, pixel operability, before and after uniformity correction (contribution from both spatial and temporal), and pixel operability. The spectral responsivity of the FPA was determined using a separate single mesa test device processed with the FPA. *NEΔT* as a function of bias and integration time at a fixed operating temperature was used as a metric for parameter optimization.

Since the QDIP is a high impedance device at operating temperature, it should yield a very high charge injection coupling efficiency into the integration capacitor of the ROIC. Charge injection efficiency can be obtained from $E_{inj} = g_m R_D /(1 + g_m R_D)$, where g_m is the transconductance of the MOSFET obtained from the measured dark current by using the expression $g_m = eI_{Det}/kT$. The dynamic resistance R_D of the detector and ROIC is calculated from $R_D.C_{ROIC} = t_{int}$, where C_{ROIC} is the capacitance of the ROIC integration capacitor, and t_{int} is the integration time. The measured differential resistance R_{Det} of the 23x23 μm^2 pixels at -350 mV bias is $5.5x10^{10}$ Ohms (compared to the calculated dynamic resistance of R_D=$5.7x10^{10}$ Ohms) at T=60 K, and detector capacitance C_{Det} is $1.4x10^{-14}$ F. The detector total current (i.e., dark + photo) is I_{Det} = 17 pA under the same operating conditions. We have integrated the signal for 20 ms. The input capacitance of ISC 9803 ROIC is 350 fF, which yields R_D of $5.7x10^{10}$ Ohms. According to the equation above, the charge injection efficiency E_{inj}= 99.65% at a frame rate of 30 Hz. The FPA was back-illuminated through the flat thinned substrate membrane (thickness $\approx$ 1000 Å). This initial array gave very good images with >99% of the pixels working, demonstrating the high yield of GaAs technology. The operability was defined as the percentage of pixels having NEΔT within 3σ at 300 K background with f/2 optics and in this case operability happens to be equal to the pixel yield.

We have used the following equation to calculate the FPA NEΔT: $NE\Delta T = \sqrt{AB}/[D^*_B(dP_B/dT)\sin^2(\theta/2)]$, where D^*_B is the blackbody detectivity, dP_B/dT is the derivative of the integrated blackbody power with respect to temperature, and θ is the field of view angle [i.e., $\sin^2(\theta/2) = (4f^2+1)^{-1}$, where f is the f number of the optical system]. The background temperature T_B = 300 K, the area of the pixel A = (23 μm)^2, the f number of the optical system is 2, and the frame rate is 30 Hz. Fig. 12 shows the experimentally measured NEΔT histogram of the FPA at an operating temperature of T = 60 K, bias V_B = -350 mV at 300 K background with f/2 optics.

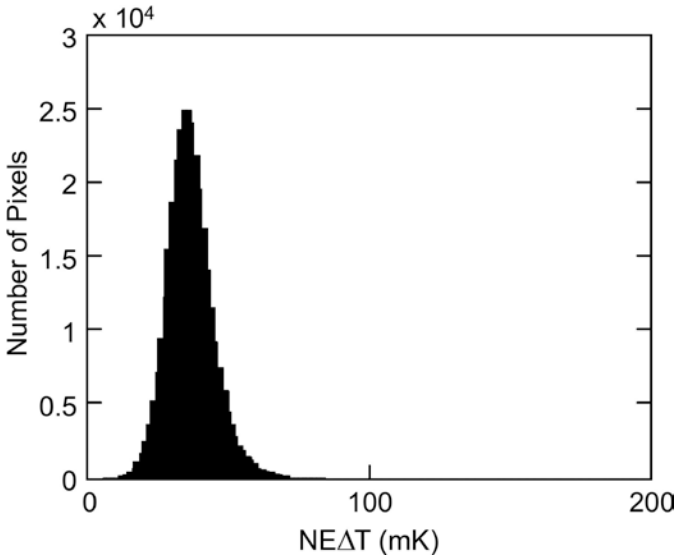

Fig. 12. Uncorrected noise equivalent temperature difference (NEΔT) histogram of the 311,040 pixels of the 640 x 512 pixel QDIP FPA. The uncorrected non-uniformity (= standard deviation/mean) of this unoptimized FPA is approximately 20%. Higher non-uniformity is attributed to the reduced number of samples collected during the experiment. The corrected non-uniformity has reduced to 0.2% after two-point correction.

The mean NEΔT value is 40 mK. This agrees reasonably well with our estimated value of 25 mK based on test structure data. The read noise of the multiplexer is 500 electrons. The experimentally measured FPA mean quantum efficiency of the FPA was 5.0%. Thus, the absorption quantum efficiency of the DWELL QDIP discussed in this paper has increased by a factor of 1.8 due to optical cavity/waveguiding effects resulting from substrate thinning. This is very similar to light coupling efficiency enhancement due to substrate thinning routinely obtained in QWIP FPAs. The experimentally measured photoconductive gain of the detector pixels at V_B = -350 mV is 0.14.

A 640x512 pixel QDIP FPA hybrid was mounted onto a 84-pin LCC and installed into a laboratory dewar which is cooled by liquid nitrogen to demonstrate a LWIR imaging camera. The FPA was cooled to 60K by pumping on liquid nitrogen and the temperature was stabilized by regulating the pressure of gaseous nitrogen. The circular cold stop of the imaging system was f/2 and the dewar window transmission was 90%. The digital data acquisition resolution of the camera is 14-bits, which determines the instantaneous dynamic range of the camera (i.e., 16,384) [5].

The measured mean NEΔT of the QDIP camera is 40 mK at an operating temperature of T = 60 K and bias V_B = -350 mV at 300 K background with f/2 optics. This is in good agreement with expected FPA sensitivity due to the practical limitations on charge handling capacity of the multiplexer, read noise, bias voltage and operating temperature. The uncorrected NEΔT non-uniformity of the 640x512 pixels FPA is about 20% (= sigma/ mean). Figure 12 shows the NEΔT histogram of this first unoptimized 640x512 pixel QDIP FPA and the higher sigma/mean was due to the reduced number of samples acquired during the measurement. The number of samples was reduced by a factor of 16 due to the high 1/f noise of the data acquisition system used during this experiment. The non-uniformity after two-point (17˚ and 27˚ Celsius) correction improves to less than 0.2%. The corrected non-uniformity could be reduced if we use a measurement system with lower 1/f noise.

Video images were taken at a frame rate of 30 Hz at temperatures as high as T = 60 K using a ROIC capacitor having a maximum charge capacity of $11x10^6$ electrons (the maximum number of photoelectrons and dark electrons that can be counted in the integration time of each detector pixel). Fig. 13 shows an image taken with this long-wavelength 640x512 pixels QDIP camera.

Fig. 13. An image taken with the first 640x512 pixels QDIP LWIR focal plane array imaging system with an f/2 AR coated germanium optical assembly.

11. SUPERLATTICE DETECTORS

The closely lattice-matched material system of InAs, GaSb, and AlSb, commonly referred to as the 6.1Å material system, has emerged as a fertile ground for the development of new solid-state devices. The flexibility of the system in simultaneously permitting type-I, type-II staggered, and type-II broken-gap band alignments has been the basis for many novel, high-performance heterostructure devices in recent years, including the GaInSb/InAs type-II strained layer superlattice infrared detectors proposed by Smith and Mailhiot [6] in 1987. The type-II superlattice design promises optical properties comparable to HgCdTe, better uniformity, reduced tunneling currents, suppressed Auger recombination, and normal incidence operation [6,7]. As illustrated in Fig. 4, the band-gap of a type-II strained layer superlattice (SLS) is determined by the energy separation between the first conduction miniband and the top-most heavy-hole miniband, rather than the band-gap of a bulk material. Hence, the SLS structure can be tailored by adjusting constituent layer thicknesses and compositions to cover a wide wavelength range for infrared detection.

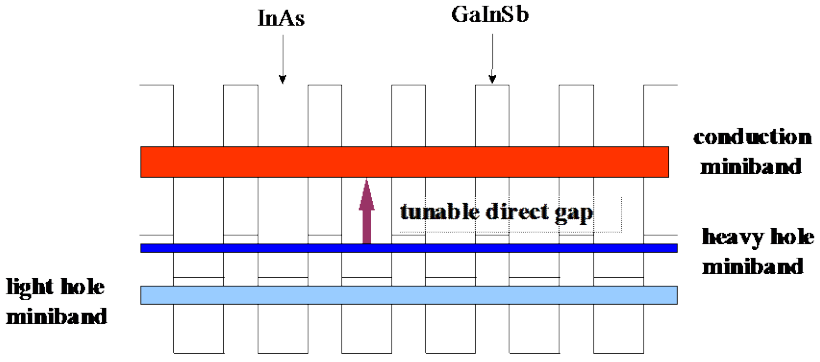

Fig. 14. Schematic energy band diagram of a short period InAs/GaInSb strained layer superlattice.

In the type-II SLS, heavy-holes are largely confined to the GaInSb layers and electrons are primarily confined to the InAs layers. However, because of the relatively low electron mass in InAs, the electron wavefunctions extend considerably beyond the interfaces and have significant overlap with heavy-hole wavefunctions. Hence, significant absorption is possible at the minigap energy (shown in Fig. 4 with the vertical arrow), which is tunable by changing

layer thickness. It is also possible to obtain large optical absorption coefficients at cutoff wavelengths as from the SWIR to as long as ~20 μm by taking advantage of internal lattice-mismatch-induced strains in the InAs/GaInSb SLS [8]. Additionally, since the gap of each constituent bulk material is larger than the effective direct gap of the superlattice, dark currents are suppressed in comparison with their values in similar cutoff-wavelength bulk ternary alloys. Another benefit of this structure for detector applications is that normal incidence absorption is permitted by selection rules, obviating the need for grating structures or corrugations that are needed in alternative quantum-well infrared photodetectors QWIPs [9]. Finally, Auger transition rates, which place intrinsic limits on the performance of such detectors and severely impact the lifetimes found in the bulk, narrow-gap detectors, can be reduced by judicious choices for the structure's geometry and strain profile [10].

In 1990, D. H. Chow and co-workers first reported $Ga_{1-x}In_xSb/InAs$ superlattice materials with high structural quality, LWIR photoresponse, and LWIR photoluminescence [11]. After a brief lull, the field has seen rapid progress since 1997, when researchers from Fraunhofer Institute demonstrated good detectivity (approaching HgCdTe, 8-μm cutoff, 77K) [12]. Recent experimental results on such structures have shown real promise. For example, Fuchs and co-workers from the Fraunhofer Institute have demonstrated type-II InAs/GaInSb photodiodes having cutoff wavelengths ranging from 7.5 to 12 μm with performance characteristics similar to those obtained from HgCdTe-based diodes and argued that improvements in material and device quality would significantly enhance device performance [13], and research efforts led by Northwestern University have demonstrated high performance superlattice diodes with cutoff wavelengths near 20μm [14]. Extensive recent efforts on InAs/GaSb mid-wave infrared (SWIR and MWIR) superlattices have enabled the demonstration and commercialization of small format superlattice based cameras by AIM [15] and BAE.

JPL, in collaboration with Raytheon Vision Systems, has demonstrated 256x256 LWIR superlattice based imaging FPAs. In addition, JPL has also developed high-performance SWIR and MWIR SLS detectors for NASA applications. JPL's high quantum efficiency detector design consists of an 18Å InAs/ 22Å GaSb p-i-n superlattice with a doping profile optimized for high quantum efficiency and low dark current. When incorporated into an AR-coated, double-pass FPA pixel design, these detectors will have 50% to 80% quantum efficiency in the 8-10 μm range. Recent advances in straight p-i-n detectors at JPL have led to 80K R_oA values over 100 Ohm cm^2 for 10μm cutoff detectors. Recently David Ting *et al*. at JPL have demonstrated R_oA values over 14,000 Ohm cm^2 for a 9.9μm cutoff device by incorporating electron-blocking and hole-blocking unipolar barriers [16]. Furthermore, this device has shown 300K BLIP operation with f/2 optics at 87 K with blackbody D^* of $1.1x10^{11}$ cm $Hz^{1/2}/W$ (see Fig. 15).

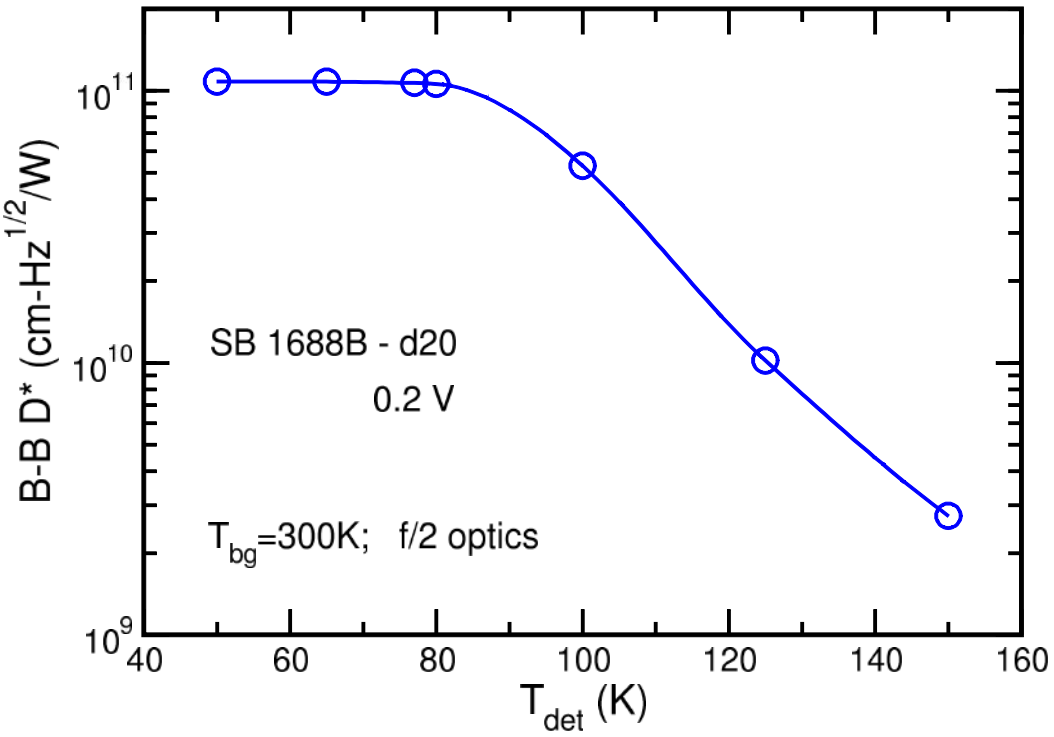

Fig. 15. Blackbody detectivity D^* of 9.9 μm cutoff superlattice complementary barrier infrared detector developed by David Ting et al. at JPL [16].

12. ACKNOWLEDGEMENTS

The authors are grateful to P. Dimotakis, T. Cwik, M. Herman, E. Kolawa, A. Larson, R. Liang, and T. Luchik for encouragement and support during the development and optimization of QWIP FPAs at the Jet Propulsion Laboratory for various applications. The research described in this paper was performed by the Jet Propulsion Laboratory, California Institute of Technology, and was sponsored by the Missile Defense Agency and the Air Force Research Laboratory.

REFERENCES

[1] H. C. Liu, F. Capasso (Eds.), Intersubband Transitions in Quantum Wells: Physics and Device Applications I and II, Academic Press, San Diego, 2000.

[2] E. L. Dereniak and G. D. Boreman Infrared Detectors and Systems, New York: John Wiley & Sons, Inc., 1996, ch. 2.

[3] S. Gunapala, S. V. Bandara, J. K. Liu, J. M. Mumolo, C. J. Hill, S. B. Rafol, D. Zalazar, J. Woolaway, P. D. LeVan, and M. Z. Tidrow, "Towards dualband megapixel QWIP focal plane arrays", Infrared Physics & Technology, Vol. **50**, pp. 217-226, 2007.

[4] S. D. Gunapala, S. V. Bandara, A. Singh, J. K. Liu, S. B. Rafol, E. M. Luong, J. M. Mumolo, N. Q. Tran, J. D. Vincent, C. A. Shott, J. Long, and P. D. LeVan, "640x486 Long-wavelength Two-color GaAs/AlGaAs Quantum Well Infrared Photodetector (QWIP) Focal Plane Array Camera" IEEE Trans. Electron Devices, Vol. **47**, pp. 963-971, 2000.

[5] S. D. Gunapala, S. V. Bandara, C. J. Hill, D. Z. Ting, J. K. Liu, S. B. Rafol, E. R. Blazejewski, J. M. Mumolo, S. A. Keo, S. Krishna, Y.-C. Chang, and C. A. Shott "640X512 pixels long-wavelength infrared (LWIR) quantum

dot infrared photodetector (QDIP) imaging focal plane array", *IEEE Journal of Quantum Electronics*, Vol. **43**, pp. 230 – 237 (2007).
[6] D.L.Smith and C.Mailhiot, J. Appl. Phys. **62**, 2545 (1987).
[7] C.Mailhiot, and D.L.Smith, J. Vac. Sci. Technol. A **7**, 445 (1989).
[8] R. H. Miles and D. H. Chow, in "*Long Wavelength Infrared Detectors*", edited by M. Razeghi, Chapter 7 (Gordon and Breach, Singapore, 1996); and references therein.
[9] S.D. Gunapala and S. V. Bandara*, Semiconductors and Semimetals* **62**, 197 (2000).
[10] C. H.Grein, P. M.Young, M. E. Flatté, and H. Ehrenreich, J. Appl. Phys. **78**, 7143 (1995).
[11] R. H. Miles, D. H. Chow, J. N. Schulman, and T. C. McGill, Appl. Phys. Lett. **57**, 801 (1990).
[12] F. Fuchs, U. Weimar, W. Pletschen, J. Schmitz, E. Ahlswede, M. Walther, J. Wagner, and P. Koidl, *Appl. Phys. Lett.* **71**, 3251 (1997).
[13] F. Fuchs, U. Weimar, E. Ahlswede, W. Pletschen, J. Schmitz, and M. Walther, *Proc. SPIE* **3287**, 14 (1998).
[14] Binh-Minh Nguyen, Darin Hoffman, Edward Kweiwei Huang, Pierre-Yves Deaunay, and Manijeh Razeghi, Appl. Phys. Lett., Vol. 93, pp. 123502 (2008).
[15] M. Walther, R. Rehm, F. Fuchs, et al., Journal of Electronic Materials 34 (6): 722-725 (2005).
[16] David Ting, Cory Hill, Alex Soibel, Sam Keo, Jason Mumolo, and Sarath Gunapala, "A high-performance long wavelength superlattice complementary barrier infrared detector" Appl. Phys. Lett., Vol. 95, pp. 023508 (2009).